

Supporting Information

Vertically Aligned Porous Organic Semiconductor Nanorod Array Photoanode for Efficient Charge Utilization

Beidou Guo,^{†,‡,§} Liangqiu Tian,^{†,‡,§} Wenjing Xie,^{†,§} Aisha Batool,^{†,‡} Guancai Xie,^{†,‡}
Qin Xiang,[†] Saad Ullah Jan,^{†,‡} Rajender Boddula[†] and Jian Ru Gong^{*,†}

[†]Chinese Academy of Sciences (CAS) Key Laboratory of Nanosystem and Hierarchy
Fabrication, CAS Center for Excellence in Nanoscience, National Center for
Nanoscience and Technology, Beijing 100190, People's Republic of China

[‡]University of CAS, Beijing 100049, People's Republic of China

[§]B.G., L.T. and W. Xie contributed equally to this work.

Experimental Section

Fabrication of photoanodes

g-CN PNR array photoanode. First, the FTO glass slides were cleaned ultrasonically in isopropanol, acetone, and ethanol sequentially, followed by N₂ drying and cleaning under N₂ plasma for 3 min. Ideally, the AAO template may directly grow on the FTO substrate; however, this method leads to the delamination of the AAO template from the substrate in the practical experiment due to the unstable Al anodization process, which may cause undesirable dissolution of the FTO substrate.¹ Therefore, according to some literature,^{1,2} a 30-nm TiO₂ thin film as an adhesion layer was sputtered on FTO and annealed in a muffle furnace at 500 °C for 2 h to obtain good crystallinity for solving the above problem. Furthermore, the semiconducting TiO₂ adhesion layer can also support a built-in electric field at the template/substrate interface, which is large enough for effective barrier layer thinning.¹ Subsequently, the Al films with various thicknesses (800, 1600, and 2500 nm) were deposited on the substrates after cleaning the surface under N₂ plasma for 3 min. Only the Al film was exposed to the solution after sealing all sides of the electrodes with silica gel. The Al film anodization was carried out in a mixed solution of 0.3 M oxalic acid (5 ml) and 0.16 M citric acid (50 ml) at 120 V, followed by soaking in 5 wt% H₃PO₄ for 3 h for pore-widening and barrier-removing at 30 °C to get the AAO template. The template was then immersed in cyanamide (Alfa Aesar, 98+%) and degassed under sonication with a power of 100 W for 10 min at 40 °C. The residual cyanamide on the surface of samples was removed by a flat quartz plate. Then the filled AAO template covered by a glass slide was wrapped by the Al foil to minimize the evaporation of the gaseous intermediate. Thenceforth, the thermal polycondensation reaction was proceeded in a tube furnace at 550 °C for 4 h (ramp: 2.5 °C min⁻¹) under Ar atmosphere. Finally, the g-CN PNR array photoanode was obtained after removal of the AAO template by chemically etching with 0.12 M NaOH for 5 h.²

g-CN NPF photoanode. The procedure of the AAO template and photoanode fabrication of NPF is the same as that of the g-CN PNR array photoanode except that the Al anodization was carried out in 5.5 wt% H₂SO₄ at 20 V, the samples were soaked

in 5 wt% H_3PO_4 for 20 min for pore-widening and barrier layer-removing at 30 °C after anodization, and the as-prepared template was applied to fabricate the g-CN NPF photoanode.

g-CN bulk film photoanode. 150 mg of the g-CN powder was ground in an agate mortar. The sample then was dispersed in ethanol (30 ml) under sonication for 2 h to get a uniform suspension. The g-CN bulk film was prepared using a drop casting technique. Specifically, 20 μl of suspension was dropped on the FTO substrate with a thin TiO_2 adhesion layer, and the electrode was dried in air. Then this step was repeated for 20 times. After that, the as-obtained electrode was annealed at 300 °C in air for 1 h to improve adhesion. This method is similar to the reported g-CN bulk control experiment.³

Characterizations

SEM images were taken from the ultrahigh resolution cold field emission scanning electron microscope (Hitachi-SU8220) at an accelerating voltage of 10 kV. Field emission transmission electron microscope (Tecnai G2F20 U-TWIN) was used to capture TEM images and EDS elemental mapping images, and the dispersed nanorods were obtained by sonication of the photoelectrode in ethanol. XRD patterns were measured on X'Pert Pro MPD. Fourier transform infrared spectrometer (Spectrum ONE) was used to collect the FTIR reflection spectra with a wavenumber range from 4000 to 450 cm^{-1} . XPS spectra measurements were carried out by X-ray photoelectron spectroscopy (ESCALAB250Xi) using an Al source. The UV-visible absorption spectra were performed on the spectrophotometer (UV-2600) equipped with an integrating sphere using BaSO_4 as the reference. The PL spectra were recorded by fluorescence spectrometer (NanoLOG-TCSPC) at 350 nm excitation. The EIS spectra of the photoanodes performance at 1.23 V_{RHE} in the range of 0.1 Hz to 100 kHz with an AC amplitude of 10 mV for the water oxidation.

PEC measurements

All the photoelectrochemical measurements were conducted using an electrochemical workstation (Zahner Zennium, Germany) in a conventional three-electrode cell with the g-CN photoanode as the working electrode, a Pt foil and a saturated Ag/AgCl as the counter electrode and the reference electrode, respectively, and 0.1 M Na₂SO₄ (pH 5.95) aqueous solution as the electrolyte without any sacrificial reagents. The samples were illuminated from the FTO (back) side under the simulated AM 1.5G sunlight (100 mW cm⁻²) generated from a 500 W Xenon lamp equipped with an AM 1.5G filter (CEL-S500, Aulight, Beijing, China) and the exposed geometrical area is 0.636 cm². And the PEC performance under illumination from the front side is slightly lower than that from the back side. The photocurrent-potential (J-V) curves were scanned at a rate of 20 mV s⁻¹ from -0.3 to 1.1 V vs. Ag/AgCl, and the potentials of the work electrodes can be calculated by the Nernst Equation (1):

$$V_{RHE} = V_{Ag/AgCl} + 0.059 \times pH + E^0_{Ag/AgCl} \quad (1)$$

where V_{RHE} is the potential vs. reversible hydrogen electrode (RHE), $V_{Ag/AgCl}$ is the potential vs. Ag/AgCl, and $E^0_{Ag/AgCl}$ is the standard potential of the saturated Ag/AgCl electrode (0.197 V at 25 °C). Mott-Schottky (MS) curves were obtained in the potential range from 0 to 1 V vs. Ag/AgCl with an AC amplitude of 5 mV under at different frequencies (2, 3, and 4 kHz) in the dark. A Si photodiode with known IPCEs is used as the reference for calculating the IPCEs of the photoanodes by Equation (2):

$$IPCE_{photoanode} = (photocurrent_{photoanode} \times IPCE_{Si}) / photocurrent_{Si} \quad (2)$$

where the photocurrent is the value of the total current under illumination minus the dark current. The stability tests were conducted in 0.1 M Na₂SO₄ aqueous solution at 1.23 V_{RHE} for 12 h.

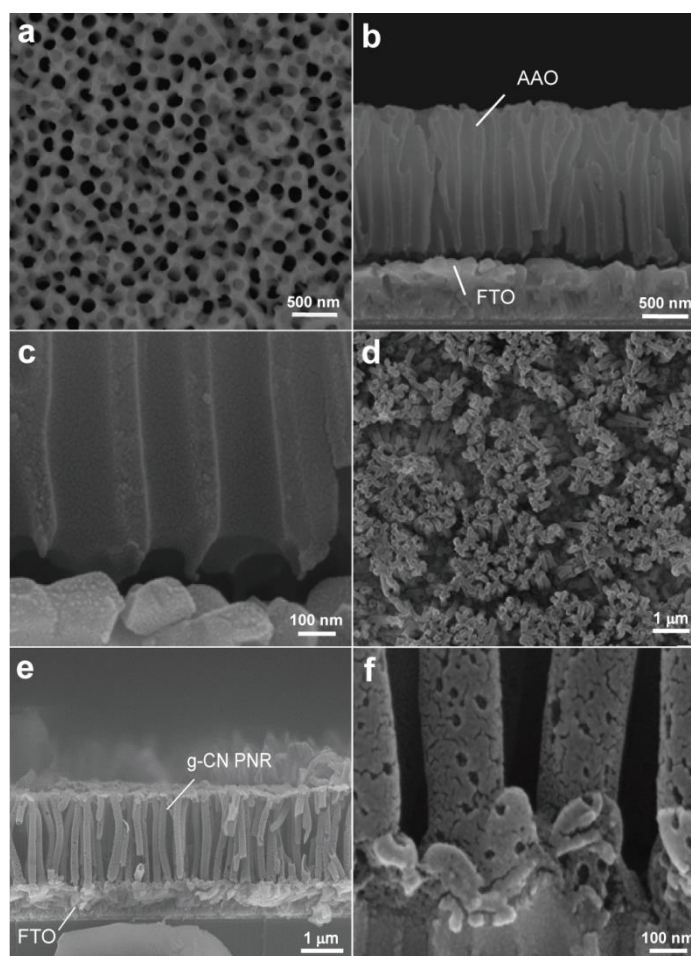


Figure S1. SEM images of the g-CN PNR array photoanode and its AAO template (height = 1600 nm). (a) A typical large-scale top-view SEM image illustrating the uniform pore structure of the AAO template. (b) The cross-sectional SEM image of the AAO template shows the oriented and cylindrical nanochannels. (c) A magnified image from (b) shows that the Al_2O_3 barrier layer between the nanochannel and the substrate is completely removed. The large-scale (d) top-view and (e) cross-sectional SEM images of the g-CN PNR array photoanode. (f) A zoomed-in SEM image from (e) displays that g-CN PNR and the substrate have an intimate contact.

The as-obtained AAO template for the g-CN PNR array photoanode with the height of 1600 nm shows a uniform nanoporous structure. The average diameter of the nanopores is about 150 nm can be observed. Most of the nanochannels in the template are perpendicular to the substrate. Meanwhile, the Al_2O_3 barrier layer between the nanochannel and the substrate is completely removed. It is difficult to see the TiO_2 adhesion layer on the FTO substrate from the SEM images, and its effect on the

photocurrent is negligible (data not shown). Finally, the vertically aligned uniform g-CN PNR array with aspect ratios in the range of 8 to 10 on the centimeter-size substrate was obtained after removal of the AAO template by chemically etching with 0.12 M NaOH.

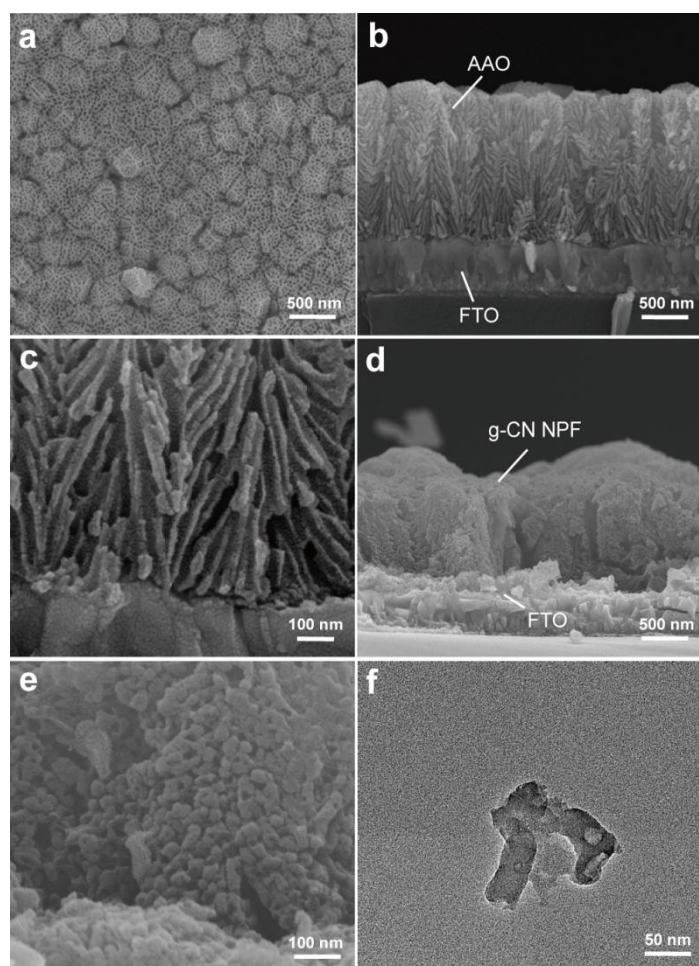


Figure S2. SEM and TEM images of the g-CN NPF coated photoanode and its AAO template (height = 1600 nm). (a) A typical large-scale top-view SEM image illustrating the uniform pore structure of the AAO template. (b) The cross-sectional SEM image of the AAO template shows discontinuous nanochannels with many branches. (c) A magnified image from (b) shows that the Al_2O_3 barrier layer between the nanochannel and the substrate is completely removed. (d) A typical cross-sectional SEM image of the g-CN NPF coated photoanode (height = 1600 nm). (e) A zoomed-in SEM image from (d) displays the aggregated nanoparticles. (f) A high-resolution TEM image of the single nanoparticles in NPF.

The prepared AAO template for the g-CN NPF coated photoanode is composed of discontinuous nanochannels with many branches. Both the length of nanochannels and the diameter of the template are in a range of 20 to 40 nm, much shorter than those of the g-CN PNR array photoanode. In addition, the Al₂O₃ barrier layer between the nanochannel and the substrate is completely removed. The g-CN NPF can also be formed in the nanochannels of the AAO template after thermal polycondensation reaction. The dendritic structure collapsed after removing the template due to its discontinuous nanochannels, forming the nanoparticle film with the single particle size of tens of nanometers.

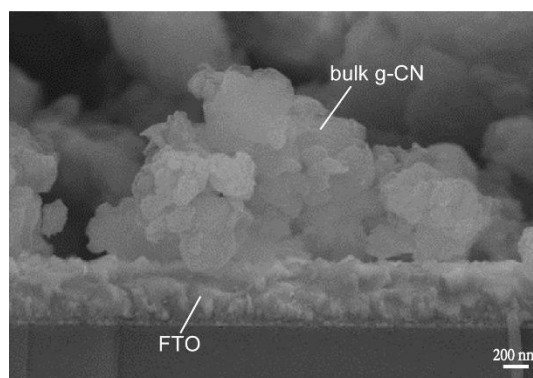


Figure S3. A cross-sectional SEM image of the g-CN bulk film coated photoanode.

Figure S3 shows that the inhomogeneous g-CN bulk film composed of aggregated bulk powders cannot fully cover the surface of the FTO substrate. Therefore, this photoanode does not have an intimate contact between the g-CN bulk film and the FTO substrate, which deteriorates its PEC performance.

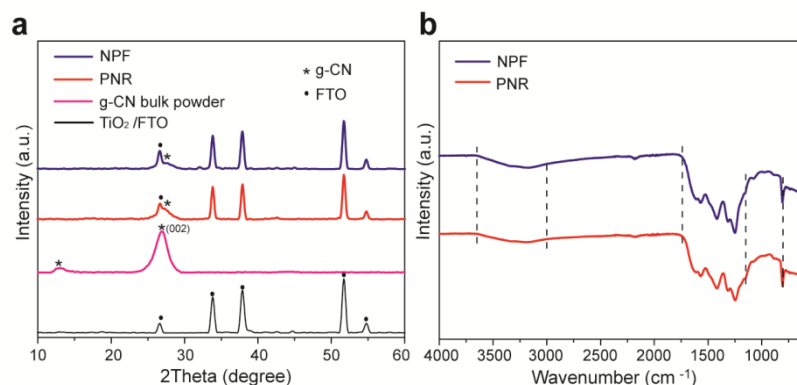


Figure S4. Structure characterizations of the designed photoanodes. (a) XRD patterns of g-CN PNR and NPF anodes, g-CN bulk powder and TiO₂/FTO. (b) FTIR spectra of g-CN PNR and NPF anodes. The typical peaks or regions are highlighted by dashed lines.

Figure S4a shows the XRD patterns of all the samples. For TiO₂/FTO, there are only several FTO characteristic peaks; a probable reason is that TiO₂ is too thin to be detected. Two typical peaks of g-CN can be clearly observed in the g-CN bulk powder: one peak corresponding to an in-plane structural packing motif is observed at 13.1°, while the other characteristic (002) peak is centered at 27.0°. However, due to the strong diffraction of the substrate (FTO), the typical peaks for g-CN are difficult to observe in both PNR (PNR/TiO₂/FTO) and NPF (NPF/TiO₂/FTO). Only a minor peak could be identified around 27.1°, which is ascribed to the stacking of conjugated aromatic systems in g-CN. These XRD results of PNR and NPF are similar with a reported g-CN sample which was also grown on FTO.⁴

Figure S4b shows the chemical bonds and functional groups of PNR and NPF in FTIR analysis. For PNR, the characteristic peaks located at 804 and 1150-1740 cm⁻¹ are attributed to the out-of-plane bending vibration of heptazine units and the stretching vibration of aromatic C-N heterocycles, respectively, indicating the formation of the basic C-N heterocycle structure of g-CN.⁵ Meanwhile, the band of 3000 to 3650 cm⁻¹ corresponds to -NH- stretching, and the signal at 2188 cm⁻¹ can be assigned to the vibration of the cyanide group.⁶ For NPF, the FTIR spectrum is very similar to PNR, demonstrating it has similar chemical bonds and functional groups compared to PNR.

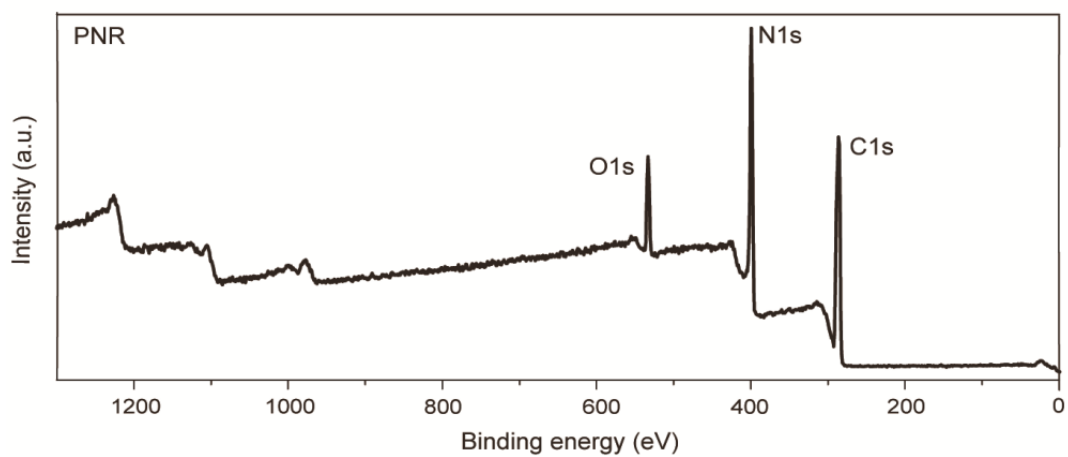


Figure S5. The survey spectrum of g-CN PNR.

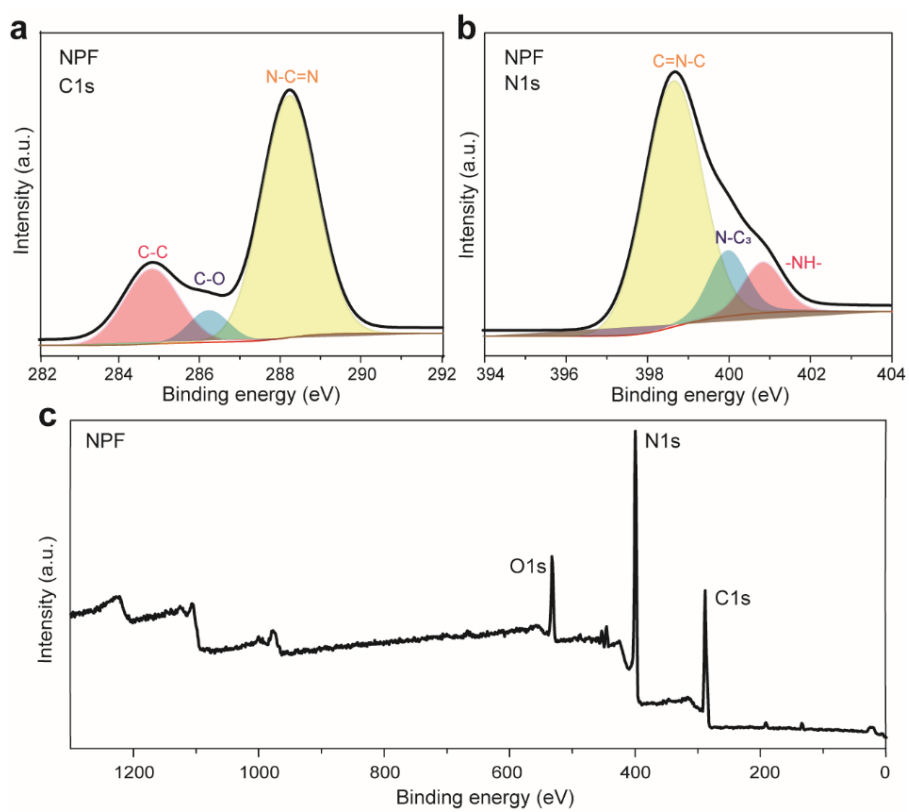


Figure S6. XPS spectra of (a) C 1s and (b) N 1s of g-CN NPF. (c) Survey spectrum of g-CN NPF.

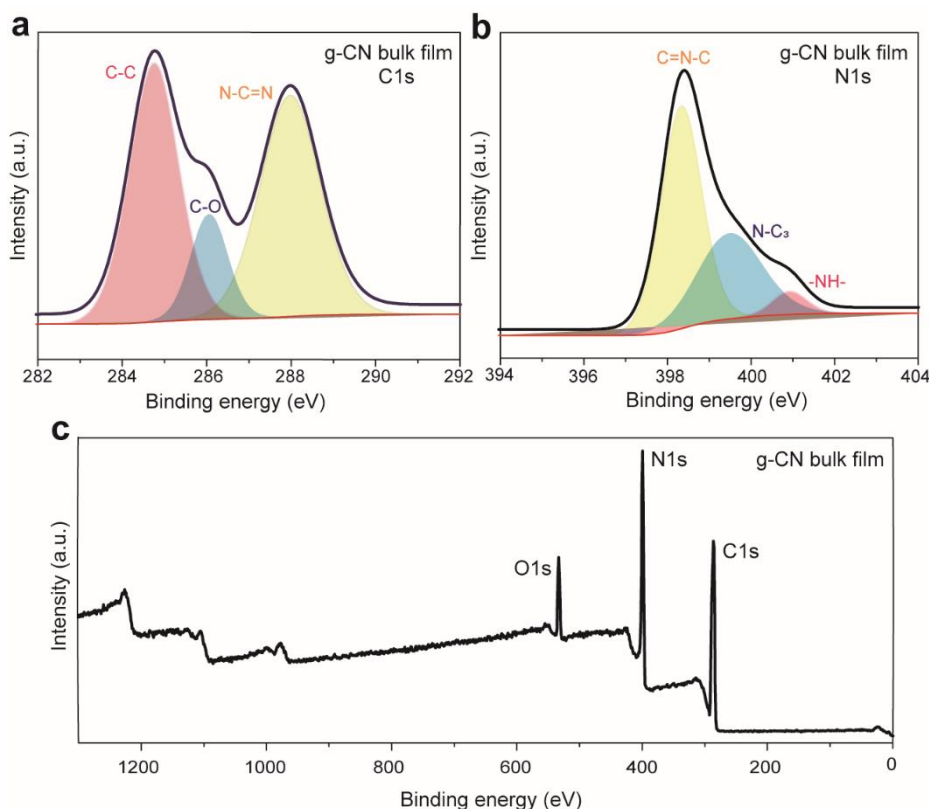


Figure S7. XPS spectra of (a) C 1s and (b) N 1s of g-CN bulk film. (c) Survey spectrum of g-CN bulk film.

The surface chemical environment of C, N composing elements in g-CN PNR, NPF and bulk film samples were investigated by XPS. For PNR, the peak at 288.36 eV in C 1s spectrum (yellow peak in Figure 2f) is attributed to the N-C=N bond and the signal of 398.81 eV in its N 1s spectrum (yellow peak in Figure 2g) is associated with the C=N-C bond, implying the formation of heptazine ring, which is the basic structure of g-CN.⁴ The deconvolution peaks in the C 1s and N 1s spectra for PNR (Figure 2f-g) and NPF (Figure S6) are extremely similar except for the small difference in their binding energies (Table S1), suggesting that PNR and NPF have extremely similar chemical structures. The attributions of deconvolution peaks for PNR, NPF and bulk film of g-CN are listed in Table S1.

Table S1. The contributions of deconvolution peaks for PNR,NPF and bulk film of g-CN.

C 1s				N 1s			
Binding energy (eV)			Bond structure	Binding energy (eV)			Bond structure
PNR	NPF	Bulk		PNR	NPF	Bulk	
284.76	284.85	284.75	C-C	398.81	398.80	398.33	C=N-C
286.31	286.41	286.06	C-O	400.11	400.26	399.49	N-C ₃
288.36	288.31	287.97	N-C=N	401.01	401.13	400.92	-NH-

The C/N ratio can be estimated by using Equation (3):

$$C / N \text{ ratio} = \frac{(\text{peak area ratio of } N - C = N) \times C \text{ at}\%}{N \text{ at}\%} \quad (3)$$

We used the peak area ratio of N-C=N in the calculation of carbon atomic percent (at%) since it is the only peak corresponding to the structure of g-CN.

The amount of -NH- can be estimated by using Equation (4):

$$\text{Amount of } -NH- \text{ (at}\%) = \frac{(\text{peak area ratio of } -NH-) \times N \text{ at}\%}{(\text{peak area ratio of } N - C = N) \times C \text{ at}\% + N \text{ at}\%} \times 100 \text{ at}\% \quad (4)$$

Since the surfaces of different g-CN samples contain O and C contaminants, we only considered the contribution of C and N from g-CN, i.e., the sum of C at% from N-C=N peak and N at%. Therefore, the amount of defects is the -NH- at% of the g-CN. The calculated results for C/N ratio and amount of -NH- in different samples are shown in Table S2.

Table S2. The C/N ratio and -NH- concentration in different g-CN samples

Sample	C/N ratio	Amount of -NH- (at%)
PNR	0.74	11.4
NPF	0.73	12.5
Bulk	1.00	2.7

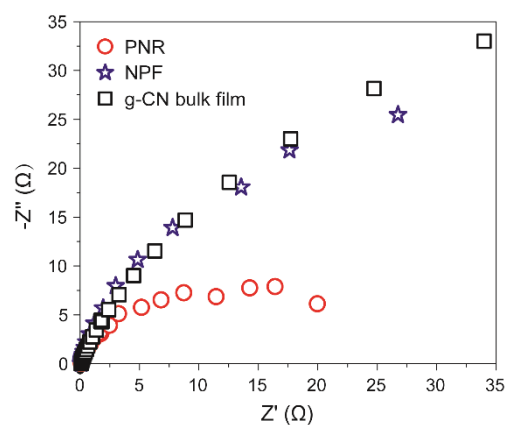


Figure S8. Nyquist plots of PNR, NPF and bulk film of g-CN photoanodes at 1.23 V_{RHE} under the illumination of simulated AM 1.5G sunlight.

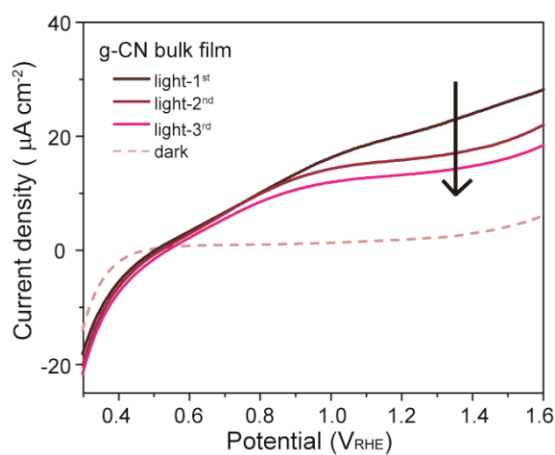


Figure S9. J-V curve of the g-CN bulk film.

It is evident that the photocurrent density keeps declining during the J-V test for g-CN bulk film. The light current decreases from 20.7 to 16.1 $\mu\text{A cm}^{-2}$ at 1.23 V_{RHE} for the second test, and it further decreases to 13.4 $\mu\text{A cm}^{-2}$ for the third test.

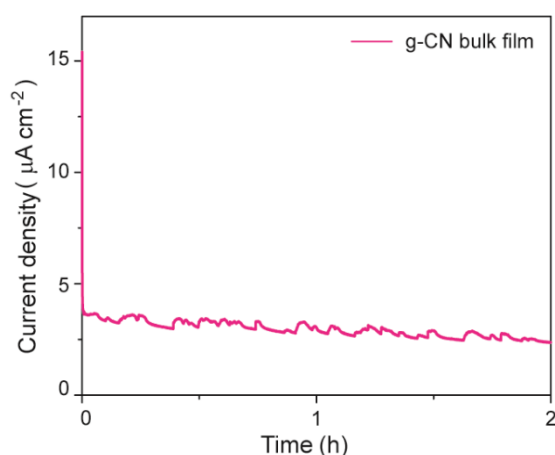


Figure S10. I-t curve of the g-CN bulk film at $1.23 V_{\text{RHE}}$ in 0.1M Na_2SO_4 solution.

The fast decay of the photocurrent density has been observed due to the seriously peeling off of the g-CN bulk film from the substrate. Figure S9 and S10 indicate that the g-CN bulk film is not stable, making it difficult to get the reliable IPCE data.

Table S3. A comparison of photocurrent density, IPCE, and stability among g-CN based polymer photoanodes without sacrificial reagents.

Photoanode	Photocurrent density ($\mu\text{A cm}^{-2}$)	IPCE @ 360 nm	Stability (h)	Electrolyte	Potential (V_{RHE})	Light source	Reference
g-CN	0.2	N/A	N/A	0.2M Na_2SO_4	1.23	200 W, > 420 nm	7
20mM Co^{2+} -CN	< 10	N/A	N/A	0.2M Na_2SO_4	1.23	50 W, > 410 nm	8
g-CN	20	N/A	N/A	0.1M KCl	~1.41	AM 1.5	9
g-CN	~30	N/A	1	0.1M Na_2SO_4	1.55	AM 1.5	3
g-CN	30.2	N/A	N/A	0.2M Na_2SO_4	1.23	500 W, > 420 nm	4
g-CN	63	< 6.6%	N/A	0.1M Na_2SO_4	1.23	AM 1.5	5
s-BCN	103.2	~12%	N/A	0.1M Na_2SO_4	1.23	AM 1.5	6
g-CN PNR	120.5	~15%	12	0.1M Na_2SO_4	1.23	AM 1.5	Our work

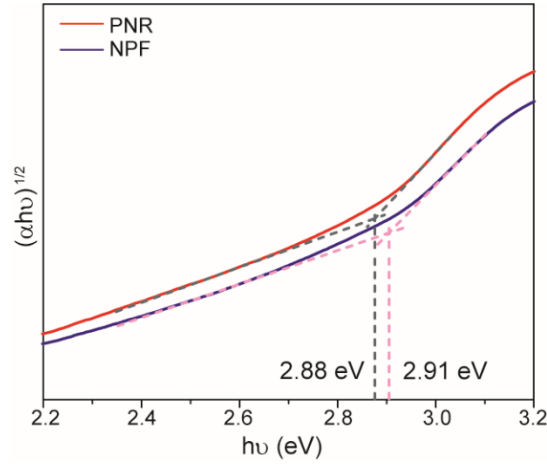


Figure S11. Tauc plots for determining the bandgaps of g-CN PNR and NPF.

Derived from the UV-visible spectra (Figure 4a) in the main text, the Tauc plots in Figure S11 show that the bandgaps of g-CN PNR and NPF are 2.88 and 2.91 eV, respectively. The absorption band edges (λ_b) can be estimated by using Equation (5):¹⁰

$$\lambda_b (nm) = \left(\frac{hc}{e} \right) / E_g = 1240 / E_g (eV) \quad (5)$$

where E_g is the bandgap; h , c and e are the Planck constant, the speed of light and the elementary charge, respectively. Therefore, the absorption band edges of g-CN PNR and NPF are 430 and 426 nm, respectively. The maximum photocurrent density ($J_{absorbed}$) of the photoanode can be calculated by Equation (6):

$$J_{absorbed} = \frac{e}{hc} \times \int_{\lambda_a}^{\lambda_b} P_{(\lambda)} A_{(\lambda)} \lambda d\lambda \quad (6)$$

where $J_{absorbed}$ is the photon absorption rate expressed as a current density, which is a constant with a fixed semiconductor photoelectrode and illumination source; λ_a is the shortest wavelength of the light emitted by the light source, λ_b is the wavelength of the absorption band edge of the photoelectrode which we calculated before, and e , h , c , P , A as well as λ are the elementary charge, the Planck constant, the speed of light, the power of incident photons, the absorbance of the photoelectrode and the wavelength of the incident monochromatic light, respectively. And, $J_{absorbed}$ for g-CN PNR and NPF are calculated to be 1.89 and 1.64 mA cm⁻², respectively.

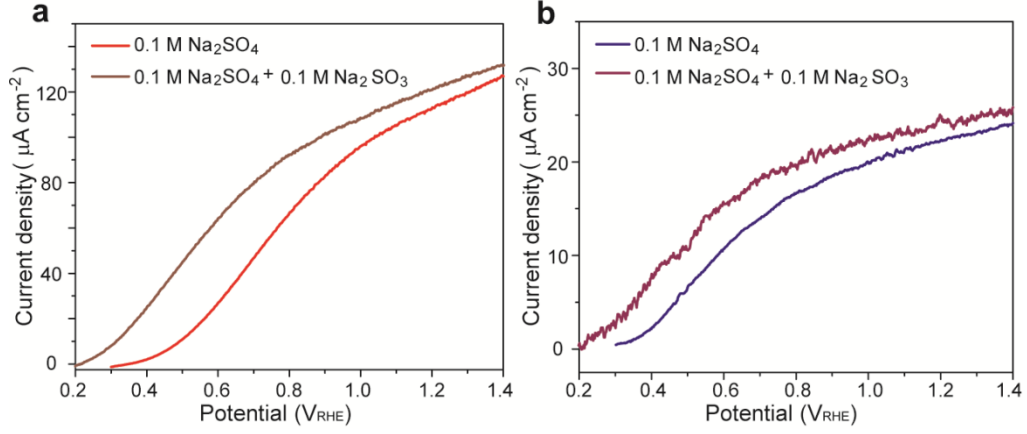


Figure S12. J-V curves for the g-CN (a) PNR and (b) NPF photoelectrodes in 0.1 M Na₂SO₄ (pH 5.95, J_{H_2O}), 0.1 M Na₂SO₄ + 0.1 M Na₂SO₃ (pH 9.92, $J_{Na_2SO_3}$).

The water splitting photocurrent can be described as Equation (7):

$$J_{H_2O} = J_{absorbed} \times \eta_{sep} \times \eta_{inj} \quad (7)$$

where $J_{absorbed}$ is the maximum photocurrent density, η_{sep} is the yield of charge separation in bulk, η_{inj} is the yield of charge injection from photoelectrode to electrolyte.

Na₂SO₃ with extremely fast oxidation kinetics can capture photogenerated holes efficiently, so the surface recombination is negligible and the injection efficiency is 100% when Na₂SO₃ is added into the electrolyte. Therefore, according to Equation (7), the η_{inj} and separation efficiency (η_{sep}) can be calculated by Equation (8) and (9)^{11,12}:

$$\eta_{inj} = J_{H_2O} / J_{Na_2SO_3} \quad (8)$$

$$\eta_{sep} = J_{Na_2SO_3} / J_{absorbed} \quad (9)$$

Herein, J_{H_2O} and $J_{Na_2SO_3}$ were acquired by subtracting the dark currents from their photocurrents under illumination.

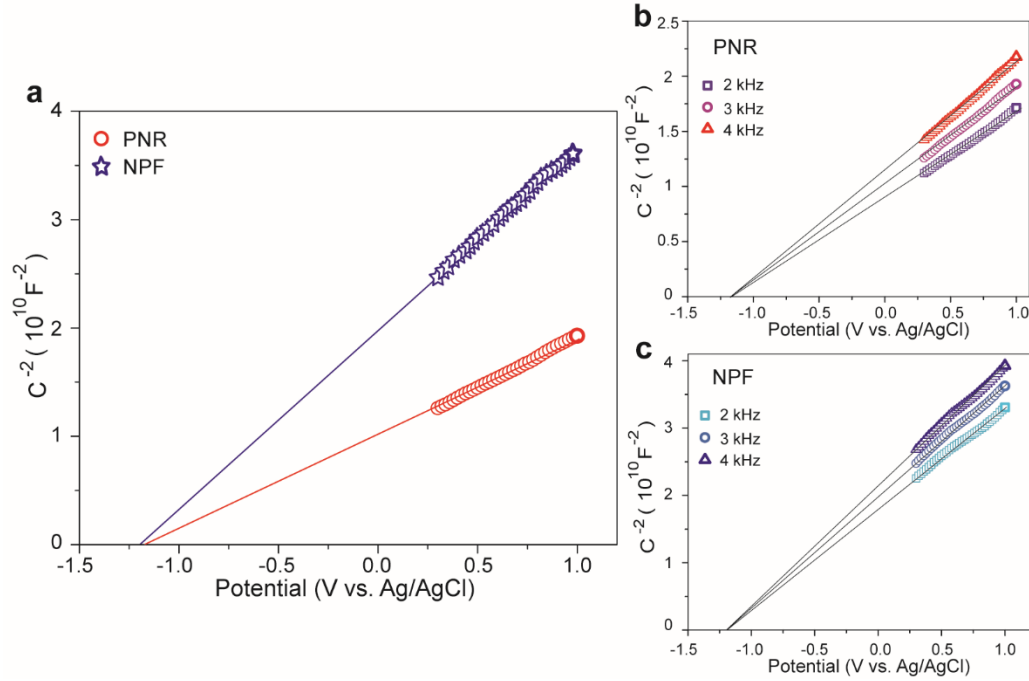


Figure S13. MS plots of photoanodes. (a) MS plots for PNR and NPF of g-CN at 3 kHz frequency. MS plots for (b) PNR and (c) NPF of g-CN at different frequencies (2, 3 and 4 kHz).

The fast decay in photocurrent density of the g-CN planar film is the result of the insufficient hole extraction,^{3,13,14} which could originate from the inadequate valence band potential level. Therefore, the energy band structures of PNR and NPF of g-CN were analyzed for the valence band potential.

The MS relationship, in theory, is derived assuming a perfectly flat electrode surface; therefore, care must be taken when analyzing the data from nanostructures with features on the scale of the depletion width. It is obvious that the flat surface condition is not met for our PNR and NPF samples. However, if the width of the space-charge layer is small compared to the radius of the semiconductor surface curvature, it is possible to approach the flat surface condition.¹⁵ In Figure S13, both g-CN PNR and NPF show a highly linear MS plot between 0.25 and 1.0 V vs. Ag/AgCl. The highly linear nature of these plots suggests that the radius of these samples is sufficiently large to avoid curvature of the plot under these conditions.¹⁶ Therefore, the flat-band potentials of these photoanodes can be obtained via extracting the intercepts of the linear parts in their MS plots. As shown in Figure S13, the flat-band potentials of PNR

and NPF were determined to be -1.17 and -1.20 V vs. Ag/AgCl (pH 5.95), respectively, coinciding with the flat-band potentials of the reported g-CN nanostructures.^{17,18} Furthermore, the MS plots of both samples display a positive slope, which is the typical characteristic of the n-type semiconductor. And the MS plots converge to the same intercept at different frequencies (Figure S13b and S13c), indicating the obtained flat-band potential (E_{fb}) is valid.

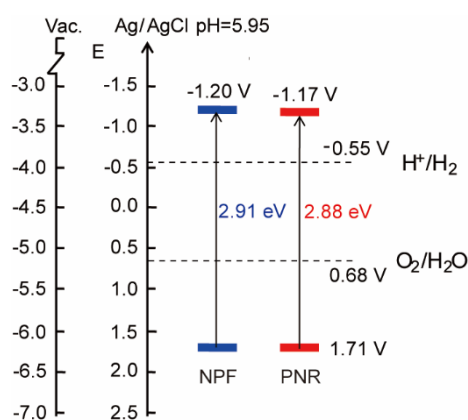


Figure S14. Schematic illustration of the energy band structures of PNR and NPF of g-CN.

For an n-type semiconductor, the conduction band potential is very close to the flat-band potential. Here, the value of the conduction band potential is approximated to the flatband potential, so the valence band potentials were determined to be 1.71 V vs. Ag/AgCl for both PNR and NPF by combining with the bandgaps derived from the Tauc plots (Figure S11), and their energy band structures are shown in Figure S14.

The g-CN bulk film has a valence band potential of ~ 1.42 V vs. Ag/AgCl,⁶ indicating that our nanostructured samples have larger OER thermodynamic driving force since our valence band potentials are more positive than that of g-CN bulk film.

REFERENCES

- (1) Foong, T. R. B.; Sellinger, A.; Hu, X. *ACS Nano*, **2008**, 2, 2250-2256.
- (2) Schierhorn, M.; Boettcher, S. W.; Kraemer, S.; Stucky, G. D.; Moskovits, M. *Nano Lett.* **2009**, 9, 3262-3267.
- (3) Bian, J.; Li, Q.; Huang, C.; Li, J.; Guo, Y.; Zaw, M.; Zhang, R.-Q. *Nano Energy* **2015**, 15, 353-361.
- (4) Liu, J.; Wang, H.; Chen, Z. P.; Moehwald, H.; Fiechter, S.; van de Krol, R.; Wen, L.; Jiang, L.; Antonietti, M. *Adv. Mater.* **2015**, 27, 712-718.
- (5) Lv, X.; Cao, M.; Shi, W.; Wang, M.; Shen, Y. *Carbon* **2017**, 117, 343-350.
- (6) Ruan, Q.; Luo, W.; Xie, J.; Wang, Y.; Liu, X.; Bai, Z.; Carmalt, C. J.; Tang, J. *Angew. Chem., Int. Ed.* **2017**, 56, 8221-8225.
- (7) Xie, X.; Fan, X.; Huang, X.; Wang, T.; He, J. *RSC Adv.* **2016**, 6, 9916-9922.
- (8) Chen, Z.; Wang, H.; Xu, J.; Liu, J. *Chem. Asian J.* **2018**, 13, 1539-1543.
- (9) Wei, X.; Jiang, H.; Liu, Z. *RSC Adv.* **2016**, 6, 81372-81377.
- (10) Cao, S.; Low, J.; Yu, J.; Jaroniec, M. *Adv. Mater.* **2015**, 27, 2150-2176.
- (11) Kim, T. W.; Choi, K. S. *Science* **2014**, 343, 990-994.
- (12) Yu, Y.; Zhang, Z.; Yin, X.; Kvit, A.; Liao, Q.; Kang, Z.; Yan, X.; Zhang, Y.; Wang, X. *Nature Energy* **2017**, 2, 17045.
- (13) Bian, J.; Xi, L.; Huang, C.; Lange, K. M.; Zhang, R.-Q.; Shalom, M. *Adv. Energy Mater.* **2016**, 6, 1600263.
- (14) Bian, J.; Xi, L.; Li, J.; Xiong, Z.; Huang, C.; Lange, K. M.; Tang, J.; Shalom, M.; Zhang, R. Q. *Chem. Asian J.* **2017**, 12, 1005-1012.
- (15) Cesar, I.; Sivula, K.; Kay, A.; Zboril, R.; Gratzel, M. *J. Phys. Chem. C* **2009**, 113, 772-782.
- (16) Franking, R.; Li, L.; Lukowski, M. A.; Meng, F.; Tan, Y.; Hamers, R. J.; Jin, S. *Energy Environ. Sci.* **2013**, 6, 500-512.
- (17) Li, Y.; Jin, R.; Xing, Y.; Li, J.; Song, S.; Liu, X.; Li, M.; Jin, R. *Adv. Energy Mater.* **2016**, 6, 1601273.
- (18) Li, X.-H.; Zhang, J.; Chen, X.; Fischer, A.; Thomas, A.; Antonietti, M.; Wang, X. *Chem. Mater.* **2011**, 23, 4344-4348.